



# GPGPU-parallelized 3D combined finite–discrete element modelling of rock fracture with adaptive contact activation approach

M. Mohammadnejad<sup>1</sup> · D. Fukuda<sup>2</sup> · H. Y. Liu<sup>1</sup> · S. Dehkhoda<sup>1,3</sup> · A. Chan<sup>1</sup>

Received: 14 June 2019 / Revised: 25 September 2019 / Accepted: 28 September 2019 / Published online: 9 October 2019  
© OWZ 2019

## Abstract

The combined finite–discrete element (FDEM) has become a well-accepted numerical technique to simulate the fracturing process of rocks under different loading conditions. However, the study on three-dimensional (3D) FDEM simulation of rock failure process is highly limited in comparison with that on two-dimensional (2D) FDEM simulations, which is due to the high computational cost of the 3D FDEM. This paper implements an adaptive contact activation approach and a mass scaling technique with critical viscous damping into a GPGPU-parallelized Y-HFDEM 2D/3D IDE code formally developed by the authors to further speed up 3D FDEM simulation besides GPGPU parallelization. It is proved that the 3D FDEM modelling with the adaptive contact activation approach is 10.8 times faster than that with the traditional full contact activation approach, while the obtained results show negligible differences. At least additional 25 times of speedups can be achieved by the mass scaling technique although further speedups are possible with bigger mass scaling coefficients chosen, which, however, will more and less affect the calculated results. Taking the advantage of the drastic speedups of the implemented adaptive contact activation approach and the mass scaling approach, the GPGPU-parallelized Y-HFDEM 3D IDE is then applied to model the fracture process of rocks in triaxial compression tests under various confining pressures. It is concluded that the GPGPU-parallelized Y-HFDEM 3D IDE is able to simulate all important characteristics of the complicated fracturing process in the triaxial compression tests of rocks including the transition from brittle to ductile behaviours of rocks with the increasing confining pressures. After that, some important aspects of the 3D FDEM simulation such as the effects of meshes, loading rates and model sizes are discussed. It is found that the mixed-mode I–II fractures are highly possible, i.e. very reasonable, failure mechanisms when unstructured meshes are used in the 3D FDEM simulation. For modelling rock fracture under quasi-static loading conditions using the 3D FDEM, the loading rate must be small enough, which is recommended to be no more than 0.2 m/s, to avoid its significant effects. Finally, it is concluded that the implementation of the adaptive contact activation approach and the mass scaling technique can further speed up 3D FDEM simulation besides the parallelization and the GPGPU-parallelized 3D IDE code with the further speedup is able to capture the complicated fracturing process of rocks under quasi-static loading conditions.

**Keywords** FDEM · Rock fracture · Triaxial compression test · Adaptive contact activation · Mass scaling

## 1 Introduction

Over recent decades, combined finite–discrete element method (FDEM), first proposed by Munjiza in 1989 with the first significant literature published in 1992 [31], has been

further developed and applied in the field of rock engineering [35] due to its capability of incorporating the advantages of both continuum and discontinuum methods in terms of simulating rock fracture and fragmentation [29]. Transition from an assembly of continuum finite elements to discontinuum is facilitated by initially zero-thickness cohesive elements which are situated along the boundaries of finite elements. The cohesive elements can be inserted via two techniques. One is to insert the cohesive elements into all boundaries of the finite elements at the beginning of the analysis, which is known as the intrinsic cohesive zone model (ICZM), and the other is to adaptively insert the cohesive elements into particular boundaries of the finite elements with the help of

✉ H. Y. Liu  
Hong.Liu@utas.edu.au

<sup>1</sup> School of Engineering, College of Science and Engineering, University of Tasmania, Hobart, TAS 7001, Australia

<sup>2</sup> Division of Sustainable Resources Engineering, Faculty of Engineering, Hokkaido University, Sapporo, Japan

<sup>3</sup> Minerals Resources Business Unit, CSIRO, QCAT 1 Technology Court, Pullenvale, QLD 4069, Australia

adaptive remeshing techniques where a given failure criterion is met. The second one is referred as the extrinsic cohesive zone model (ECZM) [9]. One of the most representative FDEM code is an open-source research code, Y code [32, 34, 36], and several attempts have been made to actively extend the original code into both open access and commercial codes, such as Y-Geo [27], Y-FLOW [49, 50], IRAZU [22], Solidity [42] and HOSS with MUNROU [39]. All of the above codes are developed based on the ICZM. Moreover, the authors have developed Y-HFDEM IDE on basis of Y code [2, 23, 24, 30]. To overcome the computationally expensive issue of Y-HFDEM IDE, which is due to its original sequential programming nature, the parallel programming scheme using the general purpose graphic processing unit (GPGPU) accelerator controlled by computing unified device architecture (CUDA) C/C++ is implemented into Y-HFDEM IDE by the authors for both two-dimensional (2D) [10] and three-dimensional (3D) [11] applications. Although there are many publications on applying the 2D FDEM to simulate the fracturing process of rocks under quasi-static loading condition, there is a limited number of publications on the application of 3D FDEM. Among the 3D FDEM application, Mahabadi et al. [26] three-dimensionally simulated rock failure process of a relatively homogenous opalinus clay in uniaxial compression strength (UCS) test and Brazilian tensile strength (BTS) test using Y-Geo with a relatively large element size (2 mm for both tests) and a high loading velocity (1 m/s). In the same literature, they further reported the 3D FDEM simulation of triaxial and polyaxial compression tests of a cylindrical rock sample with a diameter of 17.4 mm and a height of 35.8 mm. Later, Lisjak et al. [22] made a considerable advancement in the 3D FDEM simulation of the UCS and BTS tests by simulating fracture process of flowstone using IRAZU, which is parallelized on the basis of GPGPU with OpenCL. The simulations were conducted under a more reasonable loading velocity of 0.1 m/s, which is ten times smaller than that employed by Mahabadi et al. [26]. However, the rock sample with a small size of 36 mm in diameter and 72 mm in height was used in the simulation of the UCS test although the employed experimental results for validation were obtained from the specimens with a diameter of 50.8 mm and a height to diameter ratio of 2:1 [44]. Ha and Grasselli [16] used IRAZU to simulate 3D BTS, UCS and triaxial compression tests of a shale, in which the element size was 3 mm and the models were loaded axially with a loading rate of 0.1 m/s. They showed that in their simulations of triaxial compression tests, shear failure became dominant with the increasing confining pressure. Guo [15] investigated the capability of his proposed 3D FDEM by modelling the BTS test of a rock with a diameter of 40 mm and a thickness of 15 mm, under different loading rates and showed that both the fracture pattern and obtained peak load were affected by the loading rate when the velocity of the loading platens was

higher than 0.01 m/s. He further simulated the fracture of a rock cubic with a length of 500 mm in the polyaxial compression test using a mesh with an average element size of 27 mm. Moreover, Euser et al. [8] applied 3D FDEM to simulate a triaxial direct shear test and compared the simulation with experimental observations, which showed good agreement. On the other hand, Hamdi [17] employed ELFEN 3D, which is a commercial FDEM code based on the extrinsic cohesive zone model (ECZM) [51], to simulate UCS and BTS tests of a typical granite, although the fracture plane is too difficult to distinguish in their reported results of UCS simulation. It should be noted that mass scaling technique was employed by Hamdi [17] to reduce the simulation time of the 3D FDEM simulations of the UCS and BTS tests. Finally, the 3D FDEM simulation of the dynamic fracture of rocks in the BTS test under dynamic load, such as that in split Hopkinson bar pressure testing system, was only investigated by Rougier et al. [38] and the authors [11]. In sum, the literature review above concludes that the application of 3D FDEM in simulating the failure of rocks under both quasi-static and dynamic conditions is very limited, which is due to the intensive computational nature of the 3D FDEM. In some of the literatures reviewed above, 3D numerical models with smaller size than that in the standard by ISRM [20] were prevalently employed to simulate UCS and triaxial tests of rocks, which helps reduce the computational time since, with the same platen speed, nominal strain rate increases as the specimen becomes smaller, while the input parameters were calibrated against laboratory tests on the specimen of standard size suggested by ISRM [20]. The reason why the rock sample size is highlighted here is that the principle of FDEM modelling rock fracture is based on the cohesive zone model and it has already been shown that the CZM is sensitive to the specimen size and loading rate [40]. Therefore, a realistic 3D FDEM simulation of the UCS test requires to take into account not only the element size and the loading rate but also the specimen size. The realistic 3D FDEM simulation of UCS test of rocks with increasing sample size requires more computational time if a reasonably small element size and loading rate are used to mesh and load, respectively, the rock specimens. The simulation becomes more computationally expensive when 3D FDEM is applied to simulate triaxial compression tests with high confining pressures since, with the loading rate kept the same, more computational steps are needed to model the failure of rock with high strength. Meanwhile, the 3D FDEM simulation of the triaxial compression test is necessary to calibrate the input cohesion and internal friction angle of rocks beside the UCS and BTS tests [45]. Therefore, some remedies rather than using small samples and large elements, which can affect the results of simulations based on the CZM principles, should be used to make 3D FDEM simulation of triaxial compression tests more affordable. While the parallelization scheme based on

multi-core CPUs and/or GPGPU is required to speed up the 3D FDEM simulation, some other techniques such as adaptive contact activation approach and mass scaling may be used to further reduce the simulation time, too. As a matter of fact, in the application of FDEM for modelling solid fracturing including rock fracture, there has been a mystery about the timing of contact detection activation. For example, as is evident from Tatone and Grasselli [45], both Y-GEO (2D/3D) and Irazu (2D/3D) put all the solid elements (triangle elements for 2D and tetrahedral elements for 3D) into the list of contact candidate from the onset of FDEM simulation. Hereafter, this is called as the full contact activation approach. On the other hand, Guo [15] proposed to put selected solid elements and those around the newly broken cohesive elements into the list of contact candidate, which, hereafter, is called as the adaptive contact activation approach. However, the authors cannot find any literature comparing the results obtained using the full and adaptive contact activation approaches. In fact, Fukuda et al. [11] clarified that the adaptive contact activation approach could not be applied to FDEM simulation of the dynamic Brazilian test with split Hopkinson bar apparatus due to the occurrence of spurious mode, i.e. numerical instability. However, the adaptive contact activation approach may be applied for FDEM analysis of the fracture process of rocks under the quasi-static loading conditions with critical damping scheme. Thus, if the adaptive contact activation approach can be proven to generate accurate results compared with the full contact activation approach, the computational time of the FDEM simulation can be drastically reduced. Moreover, except the purpose of stabilizing the FDEM simulation in the ICZM scheme, the authors could not find any physically meaningful reason to use the full contact activation approach, especially during the intact rock deformation regime, since the rock intact deformation should be expressed by the deformation of continuum solid elements and artificial intact behaviour of the cohesive elements. In this aspect, the adaptive contact activation approach is more physically reasonable. In any case, the obtained results such as stress distribution and fracture pattern need to remain almost unaffected by the introduction of aforementioned schemes. Besides, the applicability of mass scaling on ICZM-based FDEM has not been investigated yet, which may be used to further save the computational time of FDEM simulations.

Accordingly, this paper aims to develop an adaptive contact activation approach for the self-developed GPGPU-parallelized Y-HFDEM 3D IDE code to model quasi-static loading problems. Then, mass scaling technique is introduced to further speed up the 3D FDEM simulations under quasi-static simulations and its applicability is discussed. After that, some considerations in the 3D FDEM modelling are highlighted, and a sensitivity analysis of the effect of loading rates on 3D FDEM simulation of the failure process

of rocks under quasi-static conditions is conducted. Finally, using the GPGPU-parallelized Y-HFDEM 3D IDE equipped with the adaptive contact activation approach and mass scaling technique for further speedups, a series of triaxial compression tests is simulated, and the obtained results are compared with those from experimental observations in the literature.

## 2 GPGPU-parallelized Y-HFDEM 3D IDE with adaptive contact activation approach and mass scaling technique

The original Y-HFDEM 2D/3D IDE code was developed using object-oriented programming with visual C++ [23] based on the sequential open-source Y 2D/3D library [32, 34, 36] and OpenGL. The code has been successfully employed to simulate rock fracturing in various geotechnical engineering problems including fundamental rock mechanics tests [23], rock joint shearing tests [24], rock blasting [2] and rock cutting [30]. However, because of the nature of sequential programming, it has mainly been applied to small-scale 2D problems using relatively rough meshes. To overcome this limitation, the parallel programming scheme using the GPGPU controlled by CUDA C/C++ was implemented to develop the GPGPU-parallelized Y-HFDEM 2D/3D IDE code in recent studies by the authors for both 2D modelling [10] and 3D modelling [11]. In the GPGPU-parallelized Y-HFDEM 2D/3D IDE code, the computation on the GPGPU device is controlled through CUDA C/C++ and a greater degree of parallelism occurs within the GPGPU device itself. The detailed GPGPU parallel implementation of the Y-HFDEM 2D/3D IDE code can be found in literatures [10, 11], which is omitted here. Therefore, the GPGPU-parallelized Y-HFDEM 2D/3D IDE code can run in a completely parallel manner on the GPGPU device, and no sequential processing is necessary, except for the input and output procedures. The data transfer from the GPGPU device to the host computer is always necessary to output the analysis results, the time of which is often negligible compared to the entire simulation time for most Y-HFDEM IDE simulations. The results can be visualized in either OpenGL implemented in the Y-HFDEM IDE code or in the open-source visualization software Paraview. Besides the GPGPU parallelization, a number of other features have been implemented into the Y-HFDEM 2D/3D IDE code, which mainly includes the hyperelastic model for considering anisotropic behaviour, Mohr–Coulomb shear strength model, contact damping, contact friction, local damping, adaptive contact activation and mass scaling with viscous damping. Only adaptive contact activation approach and the mass scaling technique with viscous damping are introduced in the following section since they are mainly used in this study and

have not been studied in detail in the framework of FDEM before. The detailed computing performance analysis shows that the GPGPU-parallelized Y-HFDEM 2D/3D IDE code can achieve the maximum speedups of 128.6 [10] and 286 [11] times in the case of the 2D and 3D modellings, respectively, and has the computational complexity of  $O(N)$ , i.e. the amount of computation is proportional to the number of the elements, which proves the high computation efficiency of the GPGPU-parallelized Y-HFDEM 2D/3D IDE code.

## 2.1 Adaptive contact activation approach

Besides the parallelization, the adaptive contact activation approach can be considered as a technique to further reduce the computational cost of the time-consuming contact detection in original FDEM formulation, which has not been studied comprehensively in any literature. In this approach,

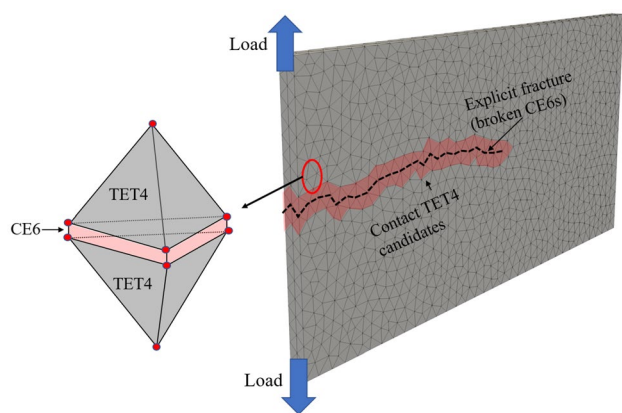
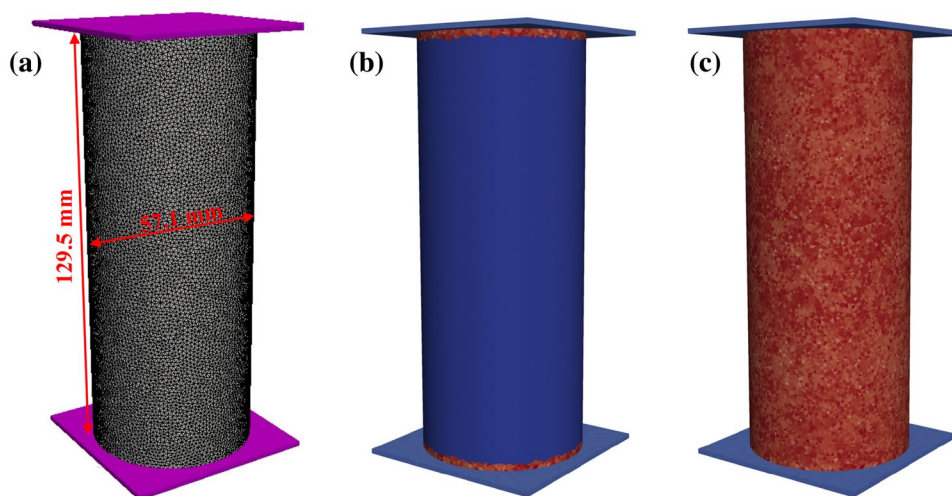


**Fig. 1** Contact activation area of TET4s around fracture in adaptive contact activation approach

**Fig. 2** Numerical modelling of UCS with adaptive and full contact activation methods: **a** numerical model, **b** adaptive contact activation modelling approach with activated contact area highlighted and **c** full contact activation modelling approach with activated contact area highlighted



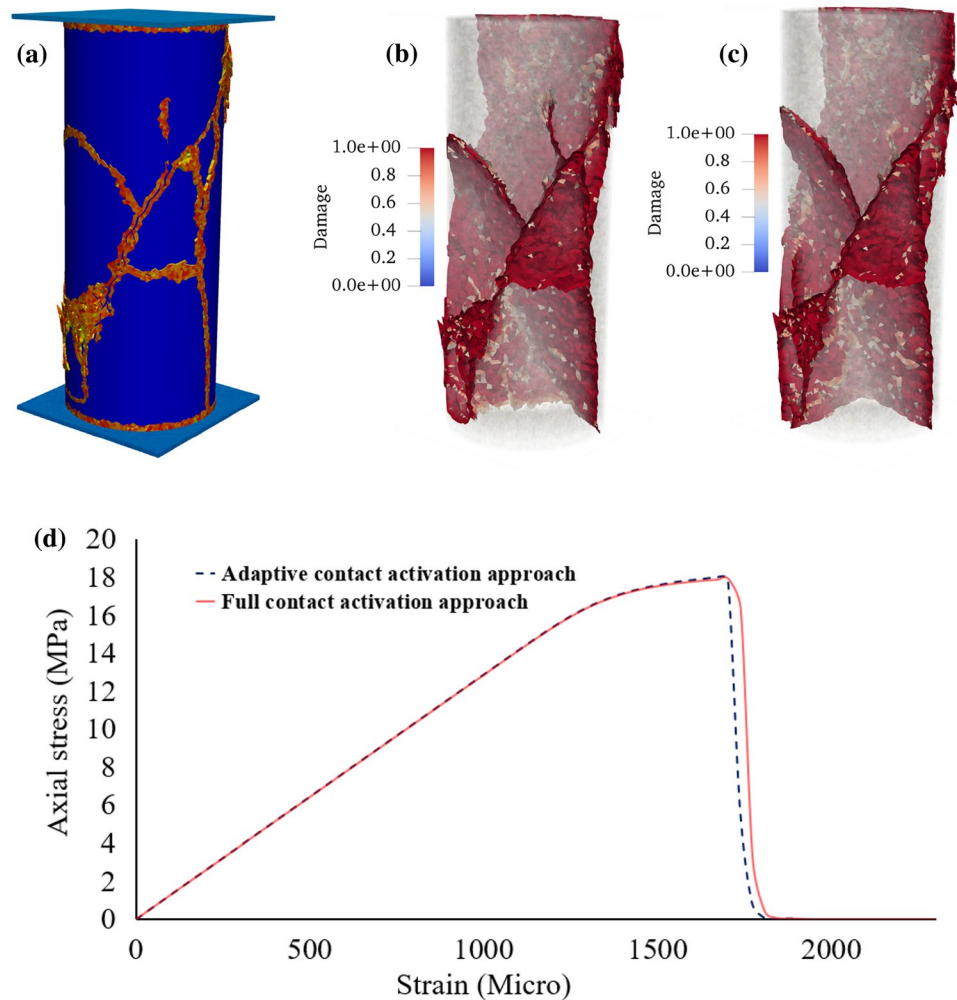
only the four-node tetrahedral finite elements (TET4s) in the vicinity of newly broken/failed six-node initially zero-thickness cohesive elements (CE6s) become contact candidates and are added to the contact detection list, as shown in Fig. 1. One advantage of the adaptive contact activation approach is that the contact detection and contact force calculations are necessary only for the initial material surfaces until the broken/failed CE6s are generated, which makes the dramatic savings of the computational time compared with the full contact activation approach.

To illustrate the capability of the adaptive contact activation approach in simulation of rock fracture process, a UCS test is simulated using both adaptive and full contact activation approaches and the obtained results are compared. The UCS model comprises a rock cylinder with a diameter of 57 mm and a height of 129 mm, which is discretized into 695,428 tetrahedral and 1,298,343 cohesive elements. Accordingly, the average element size is around 1.5 mm, which is an appropriate element size sufficient to exclude the mesh sensitivity effect for the specimen size used in the UCS test [25]. The input parameters of the UCS model are the same as those used for the triaxial compression tests detailed in Sect. 3. The rock is loaded under an effective loading rate of 0.02 m/s. In the model with the adaptive contact activation approach, the TET4s around platens are added to the contact detection list at the beginning of the simulation, while in the case of the full contact activation approach, all TET4s in the model are subjected to the contact detection. Figure 2a shows the geometry of the UCS model, and the activated contact detection areas in the models with both adaptive and full contact activation approaches are shown in Fig. 2b, c, respectively.

Figure 3a shows the activated areas of the contact candidates in the rock sample with the adaptive contact activation approach after the failure of the specimen. As shown in Fig. 3a, the TET4s around the explicit fractures are subjected



**Fig. 3** Fracture patterns and stress–strain curves from the UCS modelling with adaptive and full contact activation approaches: **a** fracture pattern with activated contact area highlighted obtained using adaptive contact activation approach, **b** final fracture pattern modelled with adaptive contact activation approach, **c** final fracture pattern modelled with full contact activation approach and **d** axial stress–strain curves modelled with both adaptive and full contact activation approaches



to the contact activation. Figure 3b, c compares the fracture patterns obtained from the models with both adaptive and full contact activation approaches, which are almost identical with very negligible differences. In Fig. 3, the damage variable,  $D$ , of CE6s considering mixed-mode I–II fracturing varies from 0 to 1, and the CE6s with  $0 < D < 1$  and  $D = 1$  can be considered as microscopically damaged and macroscopic cracking, respectively, which applies throughout this study. Further information of the damage variable can be found in the authors' former publication [11]. To further investigate the adaptive contact activation approach, Fig. 3d compares the stress–strain curves obtained from the simulations of the UCS test using the adaptive and full contact activation approaches, in which compressive stress and strain are regarded as positive and tensile stress and strain are regarded as negative. The sign convention holds true throughout this study. It is evident that the obtained stress and resultant deformation using the adaptive contact activation approach is very close to those using the full contact activation approach. Therefore, the obtained results prove the capability of the adaptive contact activation approach in

modelling rock fracture process is as good as the full contact activation approach, while the adaptive contact activation approach can reduce the simulation time significantly. The 3D modelling with the full contact activation approach takes about 15 days plus 17 h even with the GPGPU-parallelized 3D FDEM, which would take more than 12 years if a sequential FDEM code is used to complete the 3D UCS modelling using the full contact activation approach. However, it takes only 1 day and 11 h to complete the 3D UCS modelling with the adaptive contact activation approach. In other words, a speedup of 10.8 times is further achieved by the adaptive contact activation approach besides the GPGPU parallelization.

## 2.2 Mass scaling technique with critical viscous damping

The 3D FDEM is formulated in the framework of explicit FEM [32, 34, 36]. Moreover, Guo [15] showed that the time increment in 3D FDEM was mainly governed by the FEM

stability requirement rather than DEM stability requirement, which could be estimated through Eq. 1.

$$\Delta t_{\text{cr}} \approx \frac{h_{\text{min}}}{\sqrt{(\lambda + 2\mu)/\rho}} \quad (1)$$

where  $\Delta t_{\text{cr}}$  is the critical time increment,  $\lambda$  and  $\mu$  are Lamé's constants,  $\rho$  is density, and  $h_{\text{min}}$  is the minimum length of the edges of TET4s. Equation 1 can be used to estimate the time increment for 3D FDEM simulations. For 3D FDEM simulations of quasi-static problems, however, besides satisfying the requirements of numerical stability, the time increment must be chosen so that the 3D FDEM simulation is computationally affordable. The 3D FDEM simulation of rock fracturing process under quasi-static loading conditions is a very time-consuming process, which explains why it is prevalent to use high loading rates and small size models in 3D FDEM simulation of the UCS tests in some publications [22, 26]. However, as it will be demonstrated in the discussion section, both the loading rate and the model size affect the stress–strain curves and fracture patterns. Thanks to the GPGPU parallelization and the adaptive contact activation approach, most 3D FDEM simulations can be completed drastically faster than sequential codes [11]. However, when large-scale rock engineering problem is modelled using 3D FDEM, there is still a need for a technique to speed up the simulation besides the parallelization and the adaptive contact activation approach. It appeals as an affordable solution to increase the critical time increment. According to Eq. 1, the time increment is a function of the element size, density, Poisson's ratio and Young's modulus. The maximum element size is limited by the fracture process zone requirement according to CZM. Meanwhile, changing Young's modulus or Poisson's ratio results in inaccurate simulation of intact rock behaviour. The density is the only parameter which may be used to increase the time increment since the density has no physically important meaning for quasi-static loading problems. In the literatures, the artificial increase in the mass of the model is known as the mass scaling technique, which has been used in explicit FEM to increase the time increment [18]. However, the application of this technique in the 2D/3D FDEM simulations of quasi-static problems has not been investigated in detail. The main problem in the application of the mass scaling is its contradictory nature with the viscous damping concept to achieve the quasi-static stress state since the increase in the viscous damping results in the reduction in the time increment. Therefore, the applicability of the mass scaling in the frame work of the 3D FDEM is investigated in this section using the same UCS test with the same input parameters as those in Sect. 2.1, in which the density is multiplied by a mass scaling coefficient, i.e.  $m$ , and the rock is loaded under an effective loading rate of 0.02 m/s. The following mass scaling coefficients are

investigated, i.e.  $m = 1, 5, 10, 100$  and 1000, while the corresponding damping factor is accordingly adjusted according to Eq. 2, in which  $h$ ,  $\rho$  and  $E$  are the element length, density and Young's modulus, respectively.

$$\eta_{\text{critical}} = 2h\sqrt{m\rho E} \quad (2)$$

Figure 4 compares the stress–strain curves and fracture patterns obtained from the 3D FDEM simulations with various mass scaling coefficients. As shown in Fig. 4a, the effect of changing mass scaling coefficient on the stress–strain curves is less significant when the mass scaling coefficient is less than 100. However, higher mass scaling coefficient ( $m = 1000$ ) seems to initiate numerical instability. Moreover, the fracture pattern is not greatly affected by the mass scaling coefficient but fracture intensity increases with the increase in mass scaling coefficient, as shown in Fig. 4c. The mechanism of this tendency can be easily explained. In the mass scaling, since the mass in the system (and mass in each node) literally increases and since FDEM is based on the explicit time integration scheme, stress field under this slow loading condition is developed through stress wave propagation in the way that the effect of dynamic effect such as wave reflection is minimized by viscous damping. According to the elastodynamics theory, the wave speed decreases when the mass density is increased. Thus, when significant mass scaling is applied, the stresses cannot be transferred to the entire model effectively and rather pile up in the region near the loading platens. As a result, too much fracture/fragmentation is enhanced with significant mass scaling. Figure 4b depicts the relationship between the speedup times of the computational time and the mass scaling coefficients, which shows that the application of the mass scaling technique can significantly save the computational time of the 3D FDEM simulations. From the discussion above, it is concluded that a moderate increase in the mass scaling coefficient (roughly up to 10) does not significantly affect the simulation results but can significantly reduce the computing time, such as 25 times of speedups with the mass scaling coefficient of 100. Thus, the mass scaling technique with viscous damping in Eq. 2 is very useful for the 3D FDEM simulation of large-scale rock engineering applications. It should be noted that in the model with  $m = 100$ , some unrealistic cracks can be observed. In all simulations of the compression tests in the following sections,  $m = 5.0$ , and corresponding critical viscous damping is used.

### 2.3 Selection of contact penalty and artificial stiffness for cohesive element

In 3D FDEM simulations using the adaptive contact activation approach, ideally, the value of artificial stiffness of CE6s should be infinity to satisfy the elastic (intact) behaviour of rocks modelled by elastic deformation of TET4s before

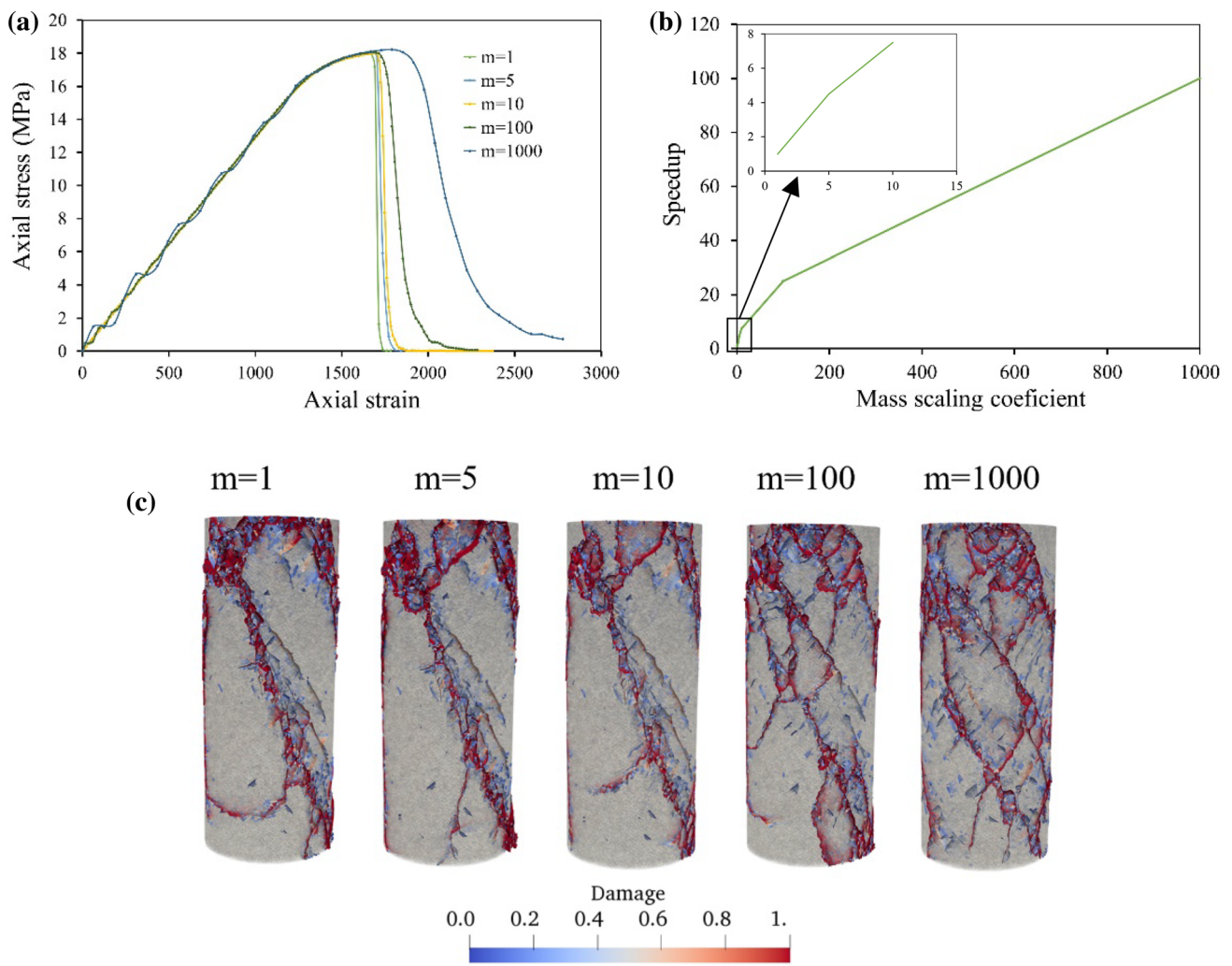


**Fig. 4** Effect of mass scaling coefficient on the simulation of UCS: **a** axial stress–strain curves obtained from the UCS modellings with various mass scaling coefficients, **b** relationship between the speedup

times and the implemented mass scaling coefficients and **c** final fracture patterns obtained from the UCS modellings with various mass scaling coefficients

any damage and failure occur. In practice, large values are used as the artificial stiffness of CE6s which are sufficient to guarantee the effectiveness of the ICZM up to the failure point. On the other hand, selecting large values for artificial stiffness of CE6s results in decreased stable time step ( $\Delta t$ ) and then longer computational time. Therefore, reasonably large values of the artificial stiffness of CE6s are required to be selected. For 2D FDEM simulations, Tatone and Grasselli [45] investigated the effect of the contact penalties between loading platens and rock and artificial stiffness of cohesive elements on elastic response of model based on the full contact activation approach. However, there are no studies on selecting these parameters for 3D FDEM simulations using the adaptive contact activation approach. To this end, the same procedure used by Tatone and Grasselli [45] for 2D modelling is followed here for 3D FDEM simulation for a UCS model using the adaptive contact activation approach.

It should be noted that in current 3D FDEM, the artificial stiffness of CE6s for their opening, overlapping and sliding are distinguished as three different parameters. Figure 5 compares the axial stress–strain curves for the intact linear elastic regime obtained for different combinations of contact penalties and artificial stiffness of CE6s (Table 1), which are selected to be proportional to the magnitude of input Young’s modulus of rock,  $E_{rock}$  in Table 2 in Sect. 3. As shown in Fig. 5, the artificial stiffness of CE6s plays an important role in the 3D FDEM modelling of the rock elastic behaviour and small values, i.e.  $1 E_{rock}$  and  $10 E_{rock}$  for the artificial stiffness of CE6s cannot model the rock elastic behaviour appropriately, while the contact penalties can be set as  $E_{rock}$ . By increasing the value of artificial stiffness of CE6s to  $100 E_{rock}$  and  $1000 E_{rock}$ , the target elastic behaviour can be precisely simulated. For the calibration purpose, the value of contact penalty numbers between loading platens

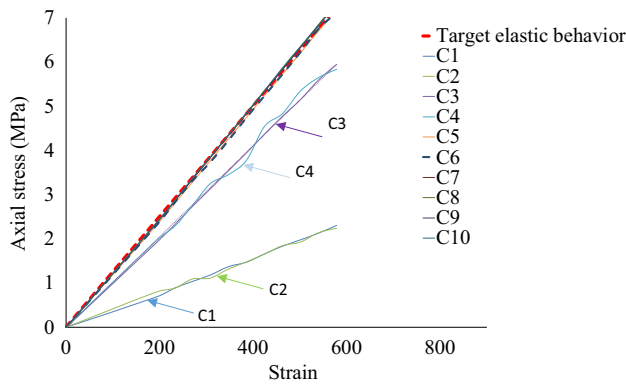


**Fig. 5** Effects of different combinations of contact penalties and artificial stiffnesses of cohesive elements on the modelled material stiffness

**Table 1** Different combinations of contact penalties and artificial stiffnesses of cohesive elements

Combination	Contact penalty		Artificial stiffness of cohesive elements	
	$P_{n\_con}$	$P_{open}$	$P_{tan}$	$P_{overlap}$
C1	$1 E_{rock}$	$1 E_{rock}$	$1 E_{rock}$	$1 E_{rock}$
C2	$10 E_{rock}$	$1 E_{rock}$	$1 E_{rock}$	$1 E_{rock}$
C3	$1 E_{rock}$	$10 E_{rock}$	$10 E_{rock}$	$10 E_{rock}$
C4	$10 E_{rock}$	$10 E_{rock}$	$10 E_{rock}$	$10 E_{rock}$
C5	$1 E_{rock}$	$100 E_{rock}$	$100 E_{rock}$	$100 E_{rock}$
C6	$10 E_{rock}$	$100 E_{rock}$	$100 E_{rock}$	$100 E_{rock}$
C7	$1 E_{rock}$	$1000 E_{rock}$	$1000 E_{rock}$	$1000 E_{rock}$
C8	$10 E_{rock}$	$1000 E_{rock}$	$1000 E_{rock}$	$1000 E_{rock}$
C9	$1 E_{rock}$	$10,000 E_{rock}$	$10,000 E_{rock}$	$10,000 E_{rock}$
C10	$10 E_{rock}$	$10,000 E_{rock}$	$10,000 E_{rock}$	$10,000 E_{rock}$

**Table 2** Input parameters of the numerical model

Parameter	Unit	Value
Density ( $\rho_{rock}$ )	kg/m <sup>3</sup>	1800
Young’s modulus ( $E_{rock}$ )	GPa	12.2
Poisson’s ratio ( $\nu_{rock}$ )	–	0.25
Tensile strength ( $T_{s\_rock}$ )	MPa	1.2
Cohesion ( $c_{rock}$ )	MPa	4.2
Internal friction angle ( $\phi_{rock}$ )	°	25
Mode I fracture energy ( $G_{fl\_rock}$ )	J/m <sup>2</sup>	2
Mode II fracture energy ( $G_{fll\_rock}$ )	J/m <sup>2</sup>	26.5
Normal contact penalty ( $P_{n\_con}$ )	GPa	122
Artificial stiffness of cohesive element ( $P_{open}, P_{tan}$ )	GPa	1220
Artificial stiffness of cohesive element ( $P_{overlap}$ )	GPa	12,200
Friction coefficient between platens and rock	–	0.1
Friction coefficient between rock surfaces generated by broken CE6s	–	0.5

and rock can be set to  $1 E_{rock}$ , while the artificial stiffness of CE6s is required to be at least more than  $100 E_{rock}$  since large values of contact penalties and artificial stiffness of CE6s can easily cause numerical instability, which eventually result in the requirement of very small time step and make the 3D FDEM simulation become unfeasible. The best combination of artificial stiffness of CE6s and contact penalties between loading platens and rock must satisfy the elastic behaviour with an appropriate time step, and the bulk elastic response of rock must not be affected by the existence of intrinsic cohesive elements up to the point of nonlinearity due to micro-crack initiation near the peak. It is found that the elastic behaviour of rock in the 3D FDEM modelling can be correctly captured when the contact penalties between loading platens and rock are chosen as 1–10 times of  $E_{rock}$  and  $P_{open}, P_{tan}$  and  $P_{overlap}$  as 100–1000 times of  $E_{rock}$  (C5–C8 in Table 1) with the reasonable time increment in mind.

### 3 3D FDEM modelling of rock failure in triaxial compression tests

In triaxial compression test, a rock cylinder is loaded axially ( $\sigma_1$ ), while a predefined confining pressure ( $\sigma_3$ ) compresses the cylinder laterally. Complex failure mechanisms occur during the triaxial compression test of the rock. Under zero and low confining pressure loading conditions, the extension of axial explicit cracks causes failure and splitting of the specimen. After peak, sudden load drop takes place and a brittle behaviour is observed. As the confining pressure increases, the triaxial compressive strength increases and faulting and shearing failure become the dominant failure mechanism. During the post-failure stage, a strain softening behaviour occurs with the load drop becoming smoother and finally a transition from brittle to ductile takes place [13]. Under high confining pressure, ductile flow occurs in rock [19].

Nonlinear behaviour and the complex fracturing mechanism of rock in the triaxial compression tests are very difficult to be addressed using conventional analytical models. Two-dimensional simulation could be a useful tool to a certain extent if used appropriately but a 3D modelling can reveal much better insights into the nonlinear behaviour and the complex failure mechanisms [6] since the corresponding fracture process is three-dimensionally complex. Although a number of efforts have been spent three-dimensionally simulating the rock fracture process in UCS, using available numerical techniques, i.e. distinct element method (3DEC) [12], finite element method (FEM) [6, 21], FEM coupled smooth particle hydrodynamics (SPH) technique [28] and particle flow code (PFC3D) [1], the number of the studies on 3D simulation of the rock fracture in the triaxial test



is very limited. Among them, Tan et al. [43] introduced a modified constitutive model based on the damage mechanics into the FLAC3D to simulate strain localization in rock specimen under different confining pressure. Baumgarten and Konietzky [3] and Akram et al. [1] employed PFC3D to investigate failure process and stress–strain behaviour of a synthetic conglomerate under triaxial loading conditions although the failure planes cannot be distinguished easily in both studies. Egert et al. [7] simulated triaxial test of sandstone using an open-source FEM software known as REDBACK but the final fracture patterns were not modelled or presented in their study. As reviewed in the introduction, there are only two reported 3D FDEM modellings of triaxial compression tests. The first was conducted by Mahabadi et al. [26] using Y-Geo with a small-sized (17.4 mm in diameter and 35.8 mm in height) sample of opalinus clay using a relatively large element size (2 mm for both tests) and a very high loading velocity (1 m/s) according to Liu and Deng [25]. As pointed out in Sect. 4.2, although using small size specimens for modelling helps to save the computation time, it may importantly impact the modelling results, similar to the effect of high loading rate. Later, Ha and Grasselli [16] simulated triaxial test of a shale using IRAZU with a diameter of 61 mm and a height of 122 mm. However, they employed an average element size of 3 mm, which is less likely to simulate the failure process correctly according to the study on the effect of the element size on FDEM simulations conducted by Liu and Deng [25]. Additionally, it has been reported that there is a limited portion of mixed-mode I–II fractures in their simulations. However, based on the CZM principle and local orientation of cohesive elements, which is to be explained in detail in Sect. 4.1, it is highly likely to capture mixed-mode I–II fractures under any loading regimes when unstructured meshes are used. Therefore, there is a need to assess the capability of the 3D FDEM in simulation of triaxial compression test. In this study, the GPGPU-parallelized Y-HFDEM 3D IDE code with the adaptive contact activation approach and the mass scaling technique is employed to conduct a series of 3D FDEM simulation of triaxial compression tests of rocks. The model comprises a rock cylinder with a diameter of 57 mm and a height of 129 mm, which is discretized into 695,428 TET4s and 1,298,343 CE6s. Accordingly, the average element size is around 1.5 mm, which is an appropriate element size sufficient to exclude the mesh sensitivity effect for the specimen size used in the triaxial compression tests according to Liu and Deng [25]. The model is loaded axially by two platens with a loading platen velocity of 0.05 m/s, while the confining pressure ( $\sigma_3$ ) increases from 0 to 15 MPa by an interval of 2.5 MPa. To further reduce the computational time in addition to the application of GPGPU parallelization with CUDA, the adaptive contact activation approach and the mass scaling technique with a mass scaling factor  $m$  of

5 and corresponding critical viscous damping factor in Eq. 2 are applied to model the fracture process of rock in triaxial compression tests. Table 2 summarizes the input parameters of the numerical model, in which the contact penalties between loading platens and rock and artificial stiffness of CE6s are determined according to the method introduced in Sect. 2, while other input parameters are determined against UCS and BTS laboratory tests of a limestone.

To maintain hydrostatic conditions, the confining pressure linearly increases up to a predefined confining pressure level with the increase in axial load. After the confining pressure reaches the target predefined level, the axial load further increases until rock failure. Figure 6i depicts the stress–strain curve from the FDEM simulation of the triaxial compression test with zero confining pressure, i.e. UCS. Figure 6ii illustrates the simulated progressive rock fracture process at different loading levels labelled A, B, C in Fig. 6i. Before the onset of nonlinearity stage, micro-cracks are initiated and randomly distributed within the rock specimen (point A in Fig. 6i). Up to this stage, the stable crack growth has occurred in the rock compared with experimental observations [46]. As the loading continues, the growth and localization of unstable microscopic cracks commence and continue until the peak stress of the stress–strain curve is reached (point B in Fig. 6i). The onset of dilatancy occurs early in this stage when the nonlinear behaviour takes place. Subsequently, the coalescence of micro-fracture forms macroscopic cracks, which results in the loss of bearing capacity of the rock specimen. The numerical simulation of the UCS test shows that the initiation and propagation of micro-cracks along loading direction lead to propagation of unstable macro-cracks, which result in creation of shearing planes (point C in Fig. 6i). The angle between the final failure plane and direction of axial load varies between 20° and 30°, which is in agreement with reported experimental observations [37]. The rapid drop in bearing capacity shows the complete failure of rock occurs due to the extension of the failure planes to the ends of specimen. Therefore, the GPGPU-parallelized Y-HFDEM IDE is able to model the process of rock failure under uniaxial loading condition including: the local initiation and growth of micro-cracks, the formation and propagation of macro-cracks and the coalescence of macro-cracks resulting in the macroscopic failure [37].

Similarly, the failure process of rock and associated differential stress–strain curve under a moderate confining pressure, i.e. 7.5 MPa, and a high confining pressure, i.e. 15 MPa, are shown in Figs. 7 and 8, respectively. Compared with the UCS test simulation, and as it was expected according to the literatures [46], both failure strength and strain of rock increase with the confining pressure increasing. Moreover, as the load increases to the ultimate load, the propagation of micro-cracks occurs quickly, and relatively a higher

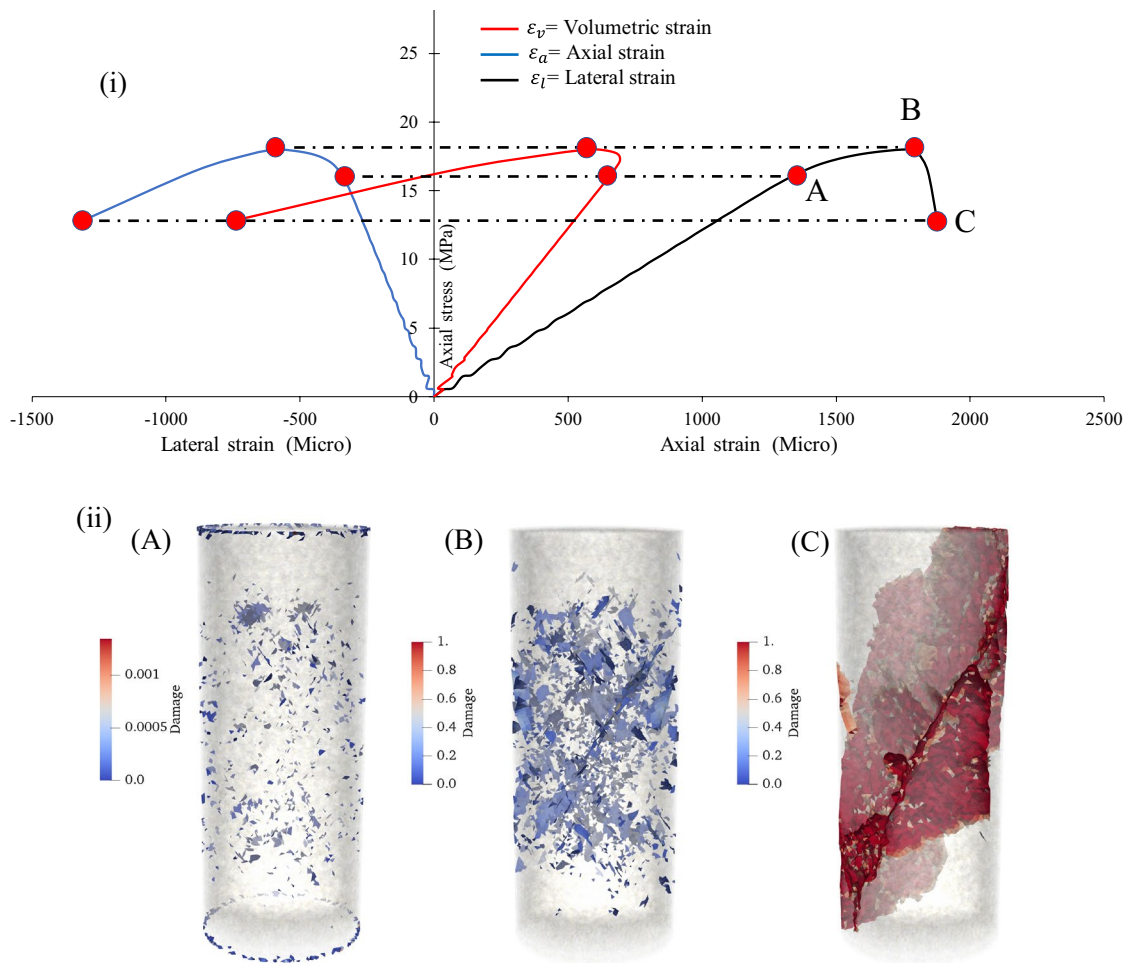


**Fig. 6** Simulation of the UCS test: **i** stress–strain curves, and **ii** rock fracture process: (A) initiation and propagation of microscopic cracks before the peak stress, (B) unstable crack propagation at the peak stress and (C) post-failure fracture pattern

number of isolated micro-cracks develop into the rock before the onset of nonlinearity stage when confining pressure is applied. As loading continues, unstable cracks initiate and propagate, which are more intense and localized in comparison with UCS test. Finally, macroscopic shear planes appear in rock after reaching to peak load.

Figure 9i compares the axial stress vs axial strain curves and the axial stress versus lateral strain curves obtained from the 3D FDEM simulations of the triaxial compression tests under various confining pressures, while the volumetric strain vs axial strain curves are shown in Fig. 9ii. As it can be seen, the mechanical behaviour of the rock specimen is significantly affected by the confining pressure. While brittle failure occurs at zero and low confining pressures, ductile failure becomes obvious in higher confining pressures. Figure 9ii shows that at zero confining pressure, i.e. the UCS condition, firstly the contraction gradually increases as the axial strain increases. Then, the dilation increases suddenly at the post-failure stage. As the confining pressure increases,

the transition from contraction to dilation becomes smoother. Figure 9iii illustrates the final fracture patterns from all the simulations of triaxial compression tests under different confining pressures. It is shown in Fig. 9iii that the specimen under zero confining pressure fails with the development of shear and near-vertical failure surfaces, which split the rock specimen into two or three parts. The failure surfaces are inclined at about  $20^{\circ}$ – $30^{\circ}$  to the axial loading direction in the uniaxial loading regime. According to Santarelli and Brown [41], rock failure in uniaxial loading condition is due to the extension of vertical failure surfaces, which stop near the ends of the rock specimen. Paterson and Wong [37] stated that both vertical and shear failure planes could occur in the uniaxial compression test. The 3D FDEM simulation illustrates the extension of both vertical and shear surfaces under uniaxial loading conditions. When the confining pressure is relatively low, i.e. 2.5 MPa, the extensional failure planes do not propagate to the ends of the rock specimen but are inclined to axial loading direction

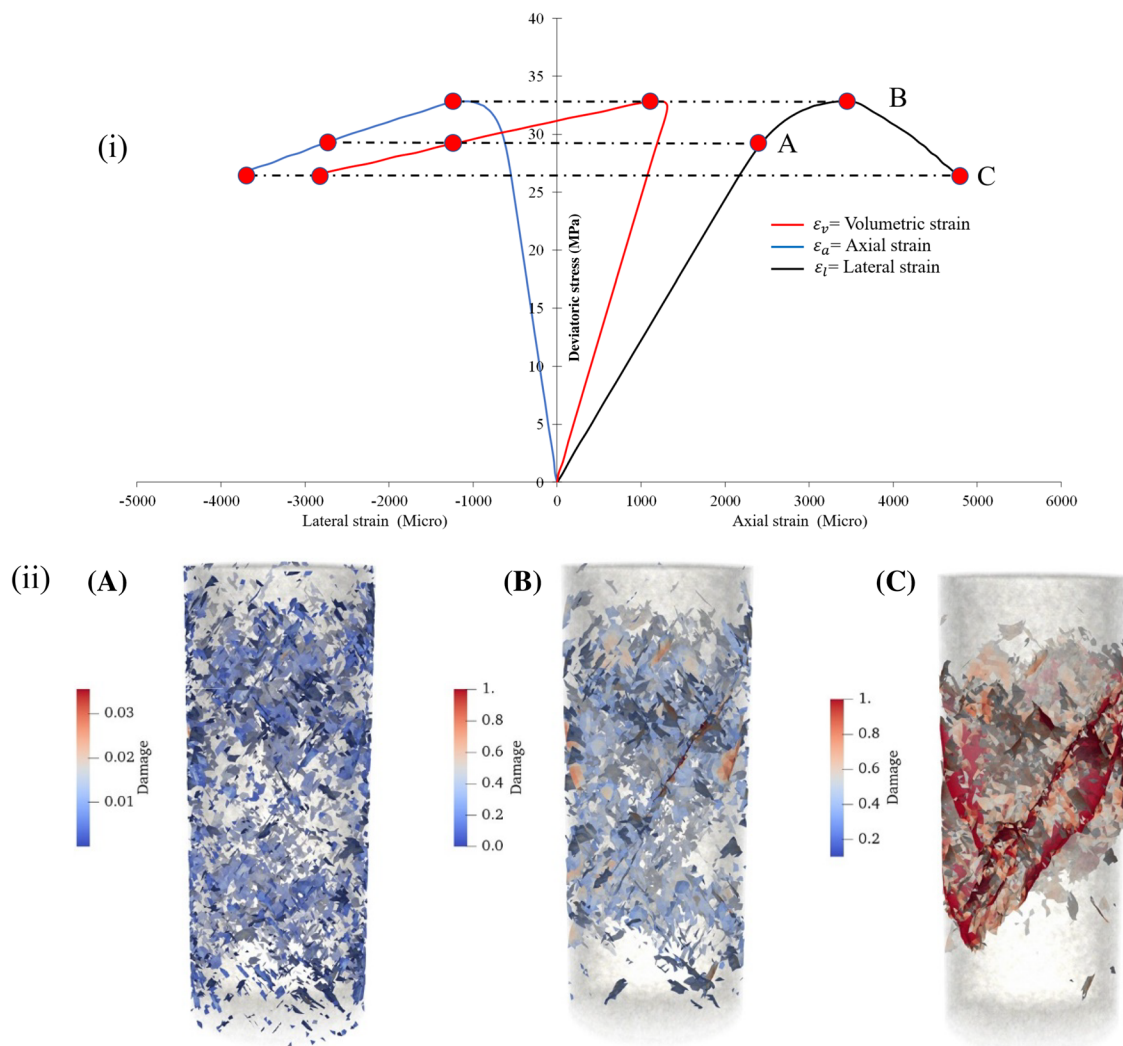


**Fig. 7** Simulation of the triaxial test with a confining pressure of 7.5 MPa: **i** stress–strain curves, and **ii** rock failure process: (A) initiation and propagation of microscopic cracks before the peak stress, (B) unstable crack propagation at the peak stress and (C) post-failure fracture pattern

with low angles. As confining pressure increases to moderate level, i.e. 5–10 MPa, several shearing planes developed at relatively larger angle, i.e.  $30^{\circ}$ – $40^{\circ}$ , inclined to the major principle stress or axial loading direction. Additionally, more failure surfaces appear in the model, which is compatible with experimental observations [41]. In the triaxial compression tests with higher confining pressures, relatively larger number of failure surfaces develop in the model, which are narrow compared with those in the case of lower confining pressures, and the failure surfaces are highly inclined to the axial loading direction. Therefore, the obtained results from the simulations show a tendency of the increase in the angle between the failure plane and the axial loading direction with the confining pressure increasing similar to the experimental observation reported by [37]. Moreover, based on the experimental observations [37], the confining pressure could cause an increase in the volume change of the specimen, as

the number of induced cracks and failure planes increases with the increase in confining pressure. This dilation behaviour, in terms of lateral and volumetric strains in Fig. 9(i–ii), is simulated well using 3D FDEM.

Figure 10 plots Mohr circles using the peak strengths obtained from the 3D FDEM simulations of the triaxial compression tests under various confining pressures, in which a failure envelope is drawn tangential to all Mohr circles. It is shown in Fig. 10 that the bulk cohesion simulated by 3D FDEM is around 5 MPa, which is 19% higher than the input cohesion of the CE6s as given in Table 2. Moreover, the bulk internal friction angle is determined as 30 degree, which is 20% higher than the input internal friction angle of the CE6s in Table 2. It should be noted that the input parameters are micromechanical parameters [45], and a combination of input micromechanical parameters, element size and mesh topology defines the resultant behaviour of the model.

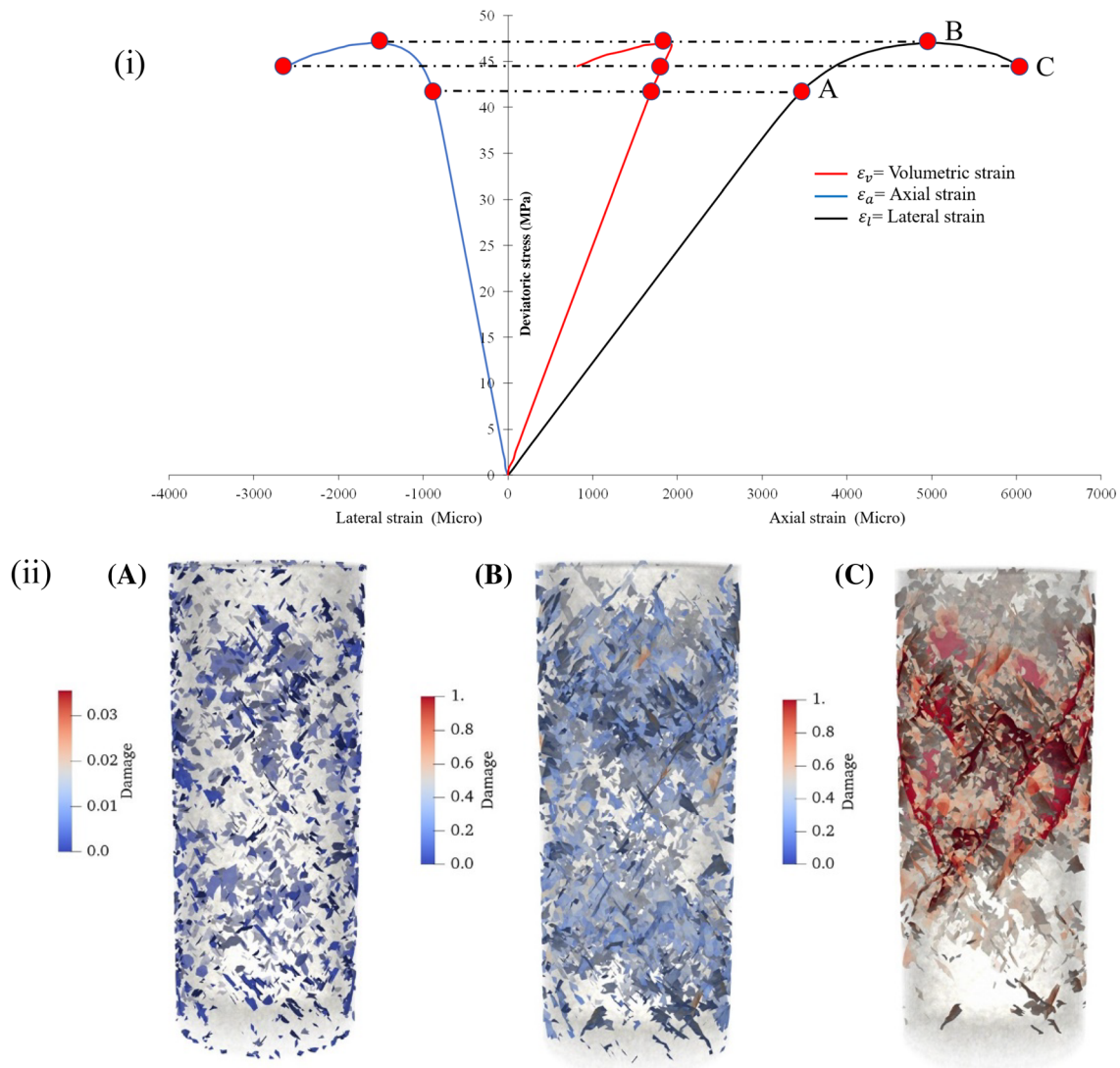


**Fig. 8** Simulation of the triaxial test with a confining pressure of 15 MPa: **i** stress–strain curves, and **ii** rock failure process: (A) initiation and propagation of microscopic cracks before the peak stress, (B) unstable crack propagation at the peak stress and (C) post-failure fracture pattern

This explanation is further supported by others' studies in literature, too. For example, Lisjak et al. [22] conducted 3D FDEM simulation of the UCS test of flowstone reported by Tatone [44], in which the input cohesion of 20 MPa as one of the micromechanical properties is about 20% higher than the obtained result of 16.4 MPa from the experiments [44], i.e. around 21.9% increase in the input cohesion compared with that from the experiment observations. Thus, the numerically simulated macroscopic behaviour of rocks should be calibrated against experimental data. The mechanism of the difference between the input micromechanical parameters and modelled macroscopic parameters is further discussed in Sect. 4. Therefore, the 3D FDEM simulation of triaxial compression test proves the capability of the Y-HFDEM IDE with the adaptive contact activation approach and the mass

scaling technique in simulating all characteristics of rocks in triaxial compression tests under various confining pressures such as the increase in rock compressive strength and strain at peak stress, softening behaviour for relatively lower confining pressure, transition from brittle to ductile and resulted failure patterns with the increase in confining pressure.

## 4 Discussion

A realistic 3D FDEM simulation of rock fracturing process relies on a good understanding of the principal of CZM and other effective factors in addition to input parameters. Besides the input parameters, there are three important issues which must be paid attention to in the 3D FDEM



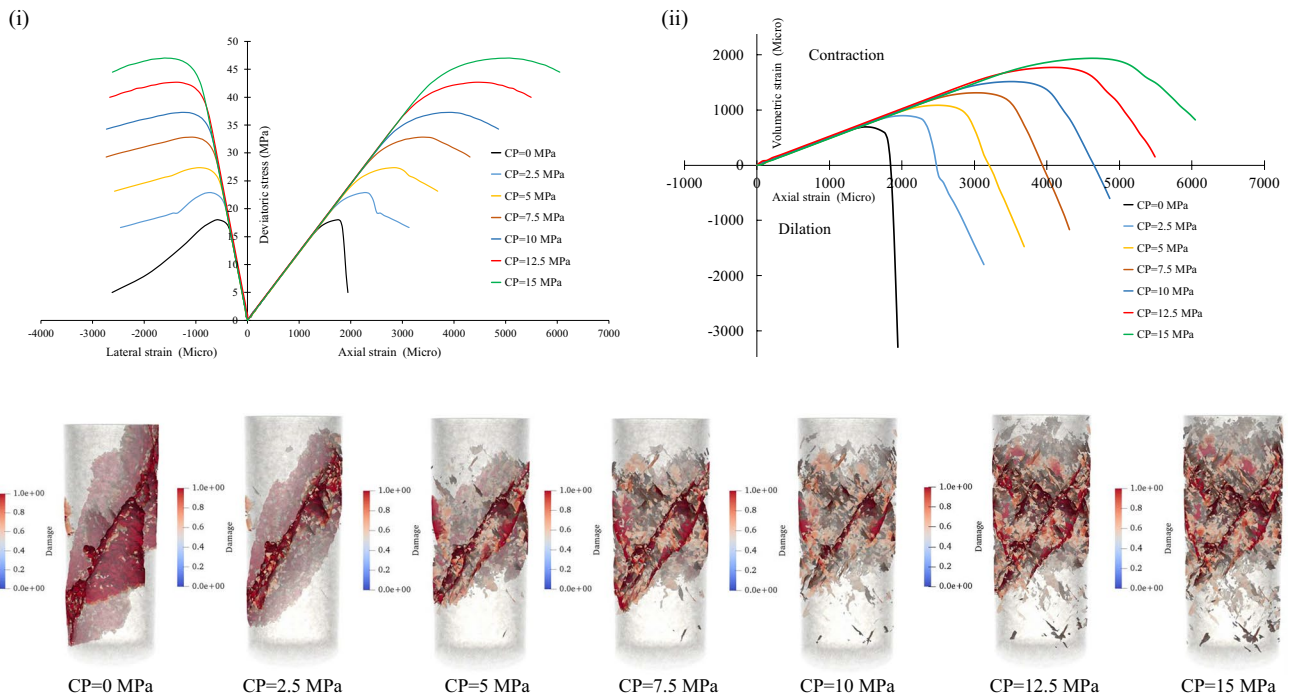


**Fig. 9** **i** Obtained stress–strain curve under different confining pressures, **ii** volumetric strain—axial curve under different confining pressures and **iii** final fracture pattern under different confining pressures (CP)

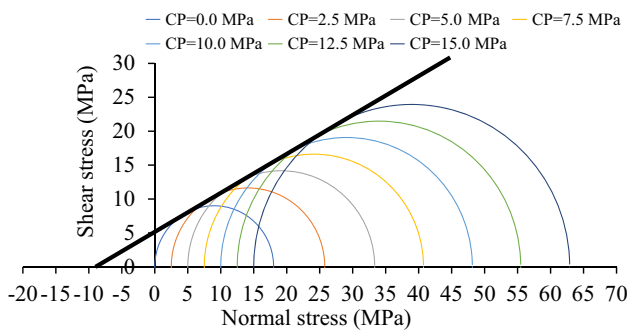


**Fig. 10** Mohr circles and shear strength envelope plot using the results from the simulation of the triaxial tests with various confining pressures (CP)

simulation of rock fracturing process. The first is the fact that the 3D FDEM method is a mesh-dependent technique, and the failure mode as well as the fracture pattern are significantly affected by element size and mesh orientation. The second factor is that the 3D FDEM is a dynamic method in nature, and the dynamic relaxation is implemented in 3D FDEM to simulate quasi-static loading conditions, in which the loading rate must be chosen correctly. The third important factor is that the computational cost of 3D FDEM simulation of rock fracturing increases with the model size since the requirement of maximum element size no bigger than the length of the fracture process zone must be satisfied in the

area where fracturing process is modelled. These important aspects are discussed in the following sections.

### 4.1 Effect of meshes

Munjiza and John [33] conducted the mesh sensitivity analysis for 2D FDEM and concluded that finite elements could increase the accuracy of the calculation of stress and strain fields near crack tip and failure loads. Camacho and Ortiz [5] proved that the mesh size dependency of the 2D cohesive model could be avoided when the mesh size was kept small enough to resolve the fracture process zone. Guo et al. [14] conducted the mesh sensitivity analyses by modelling a single tensile fracture propagation and three-point bending tests using 3D FDEM and stated that the size of the cohesive elements was required to be selected on the basis of the material properties and should not exceed a specific range. Liu and Deng [25] further investigated the effect of cohesive element size on 2D FDEM simulation of rock fracture process and concluded that very fine cohesive elements with maximum element size no bigger than the length of the fracture process zone must be used in the area where fracture process is modelled. Different numbers have been suggested as the minimum number of required elements within cohesive zone, i.e. fracture process zone, from 2 to no more than 10 elements [47]. Meanwhile, the lengths of cohesive zone ( $l_{c2}$ ) could be estimated as a function of Young modulus ( $E$ ),

critical energy release rate ( $G_c$ ) and maximum interfacial strength ( $\sigma_{\max}$ ) through Eq. 3 for different loading conditions, i.e. mode I and mode II.

$$l_{CZ} = ME \frac{G_c}{\sigma_{\max}^2} \quad (3)$$

In Eq. 3,  $M$  is a variable which varies between 0.21 and 1 [47, 48]. Therefore, the calibrated parameters against micro- and meso-scales models are not necessarily applicable for macro-scale simulations in 3D FDEM modelling, which explains the differences between the input and modelled cohesion and friction angle in the 3D FDEM modelling of triaxial compression tests in Sect. 3 although the chosen small element size satisfies the requirements discussed above. On the other hand, the chosen small elements make the 3D FDEM modelling become computationally expensive, which is made feasible thanks to the GPGPU parallelization, adaptive contact activation approach and mass scaling technique implemented into Y-HFDEM 3D IDE. For 3D FDEM simulations of large-scale engineering applications, other remedies such as multi-scale analysis may still be needed to make sure that the maximum element size is

not bigger than the length of the fracture process zone in the area where fracture process is modelled. Otherwise, the 3D FDEM simulations of the large-scale engineering applications using the input parameters identified through the calibration against laboratory-scale tests have no qualitatively and quantitatively reasonable meaning.

Moreover, unstructured meshes with cohesive elements inserted could introduce local stress or strain anisotropy and extra toughness into the 3D FDEM modelling. In terms of modelling rock materials, the induced anisotropy could be considered as an advantage rather than a disadvantage, since rock is naturally an heterogeneous material. For unstructured mesh, the influences of cohesive element size discussed above are even more evident in 3D FDEM due to three-dimensionally complex interlocking and frictional effects. In this sense, it may be unreasonable to try to capture pure mode I or mode II failures using the unstructured mesh in 3D FDEM simulation. To explain this concept in detail, Fig. 11a, b shows the topological relationships between the loading conditions and the TET4s in the cases of the structured meshes for the loading conditions causing mode I and mode II crack deformations, respectively, in which loading directions are indicated by the blue arrows. In Fig. 11,  $o$  and

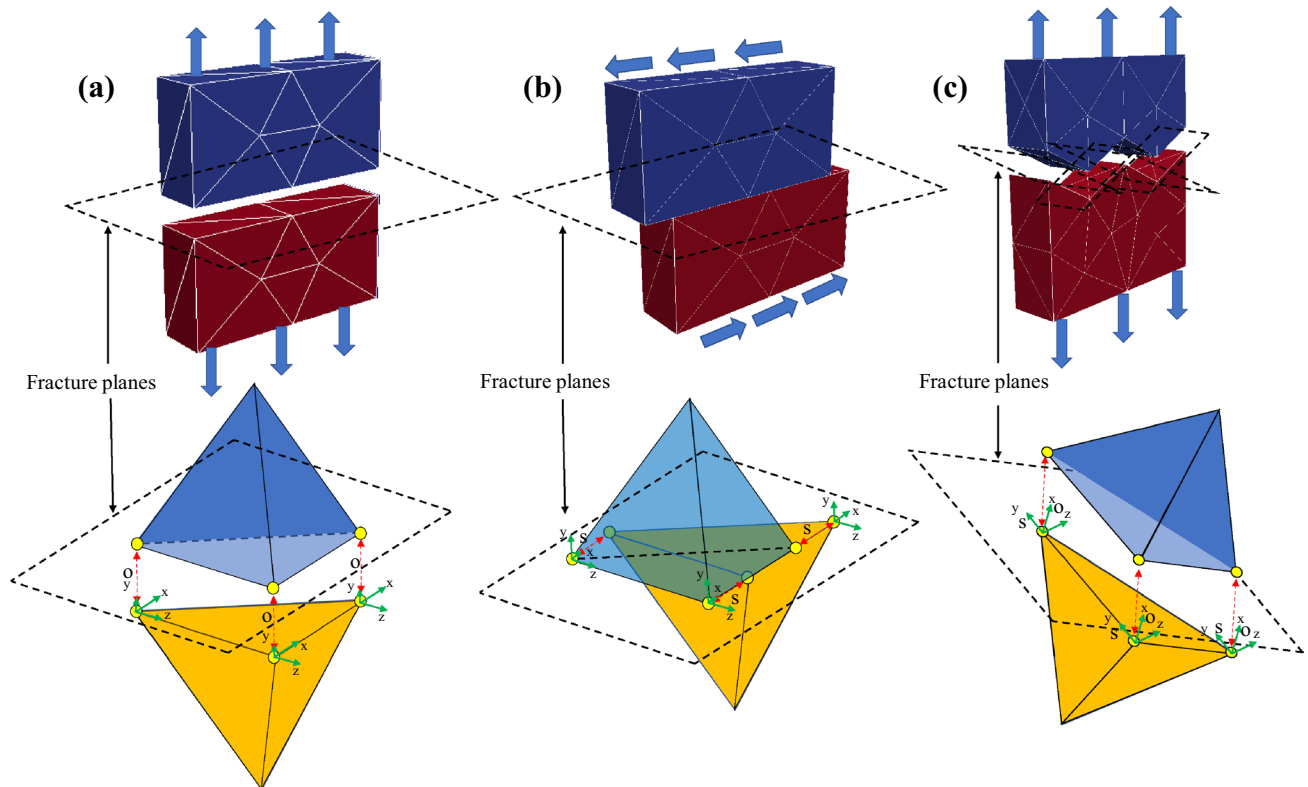


**Fig. 11** Topological relationship between local mesh alignments and local loading conditions ( $o$  and  $s$  represent opening and sliding displacements, respectively): **a** local structured elements under local loading condition causing pure mode I failure, **b** local structured ele-

ments under local loading conditions causing pure mode II failure and **c** unstructured elements under local loading condition causing mixed-mode I–II failure

$s$  represent the opening and sliding displacements, respectively, of CE6s. As shown in Fig. 11a, b, the opening and shearing displacement vectors between crack surfaces can easily take place along the boundary of TET4s in favour of local orientation of the TET4s. For example, the pure opening, i.e. pure mode I crack deformation, occurs along the vertical direction and is perpendicular to the fracture plane in Fig. 11a, while the displacements in the other directions are zero or close to zero. Figure 11b shows pure shearing condition, i.e. pure mode II crack deformation, in which the relative shear displacement between crack surfaces occurs only in the horizontal direction within  $x$ – $z$  plane and shearing is parallel to the fracture surface. Accordingly, pure mode I and mode II failures can be captured in the simulations with structured meshes if the resultant fracture plane aligns well with the structured element boundaries. However, in the case of unstructured mesh (Fig. 11c), under the same loading conditions as Fig. 11a, i.e. mode I, it is unlikely that pure mode I or II failure takes place along the TET4s' boundaries and the loading is unlikely to cause pure opening and pure shearing along the boundaries of TET4s, and the fracture plane consisting of the CE6s with random orientations are deemed to make irregular angle with respect to the loading direction indicated by the blue arrows. Hence, it is highly possible that mix mode I–II fractures are captured when unstructured elements are used in FDEM simulations. Therefore, the loading condition is not the only factor which affects the type of failure, and mesh topology plays an important role as well. Accordingly, in the interpretation of obtained results, the modelling of pure mode I and mode II fracture should be a function of element orientations in addition to loading conditions.

## 4.2 Effect of loading rates

Loading rate is another effective factor in all FDEM simulations of rock fracture process under both quasi-static and dynamic loading conditions. For quasi-static loading condition such as that in the 3D FDEM simulation of the triaxial compression tests, the correct selection of loading rate becomes a very important factor since the computational time significantly increases with the decrease in loading rate, while higher loading rate may significantly affect obtained results. Both numerical and experimental observations have revealed that the increase in the loading rate results in the increase in the energy in the testing system, micro-branching of cracks and crack speed [5, 51], fracture toughness and failure stress [4]. Mahabadi et al. [26] three-dimensionally simulated UCS and BTS tests of a relatively small rock specimen comparing to standard tests using Y-Geo with a loading velocity of 1 m/s, and the results clearly showed that multi-fracture propagation around the centre of the BTS models, which could be due to the high amount of energy

introduced into the model by the high loading velocity of 1 m/s. It is also worth mentioning that the same velocity of loading platens does not mean the same loading rate when the sample size is smaller, i.e. the increase in the strain rate with smaller sample occurs, while the simulation time can be reduced. Later, Lisjak et al. [22] improved Mahabadi et al.'s [26] simulation by applying an effective loading rate of 0.1 m/s, which seems to be more reasonable to model the quasi-static loading condition, although the size of the UCS numerical model was much smaller than the actual size of the rocks used in the laboratory experiment [44]. In addition, the generation of cracks from curved free faces of the BTS disc are found which can be considered as a typical dynamic effect in Lisjak et al. [22]. Guo [15] investigated 3D FDEM modelling of the BTS tests of rocks under different loading rates and showed that both fracture pattern and obtained peak load could be affected by the loading rate when it is higher than 0.02 m/s for the sample size of 40 mm with the average element size of 1.5 mm. This section investigates the effect of loading rate on 3D FDEM simulation and the aforementioned triaxial test with zero confining pressure, i.e. UCS of a relatively homogenous limestone, is modelled as an example, whose size is the same as that in the laboratory test. For the convenience of making comparison with the results obtained by Guo [15], which modelled the BTS tests of a sample with a diameter of 40 mm and a thickness of 15 mm, the BTS tests are also modelled using the GPGPU-parallelized 3D FDEM and the diameter of the rock sample is the same as that in the UCS test simulation, while the ratio of the thickness to the diameter is 0.5. An average element size of 1.5 mm is selected for both UCS and BTS models and the loading rates of 0.02 m/s, 0.1 m/s, 0.2 m/s and 1 m/s are applied on the models to simulate the quasi-static loading conditions with the adaptive contact activation approach. Figure 12 compares the axial stress versus axial strain curves obtained from the 3D FDEM simulations of UCS and BTS tests under different loading rates, which shows that the failure stress in the BTS simulation decreases with the decrease in loading rate, while in the UCS simulation, the decrease in the peak stress only occurs with the loading rates decreasing from 1 to 0.2 m/s although the post-failure stages are affected by the loading rates. From the fracture patterns illustrated in Fig. 13a, it can be seen that the intensity of rock fracturing increases with the increase in loading rate in the BTS simulation, especially in the regions around the central line of the model and near the platens, where multiple fracturing and even fragmentation take place, which are often observed under dynamic loading conditions. In the UCS simulation, with the loading rate increasing, a significant change of the fracture pattern has not been observed except the case with the loading rate of 1 m/s but the intensity of the fracturing is increased evidently. Therefore, the 3D FDEM UCS and BTS simulations prove that the loading rate affects both the

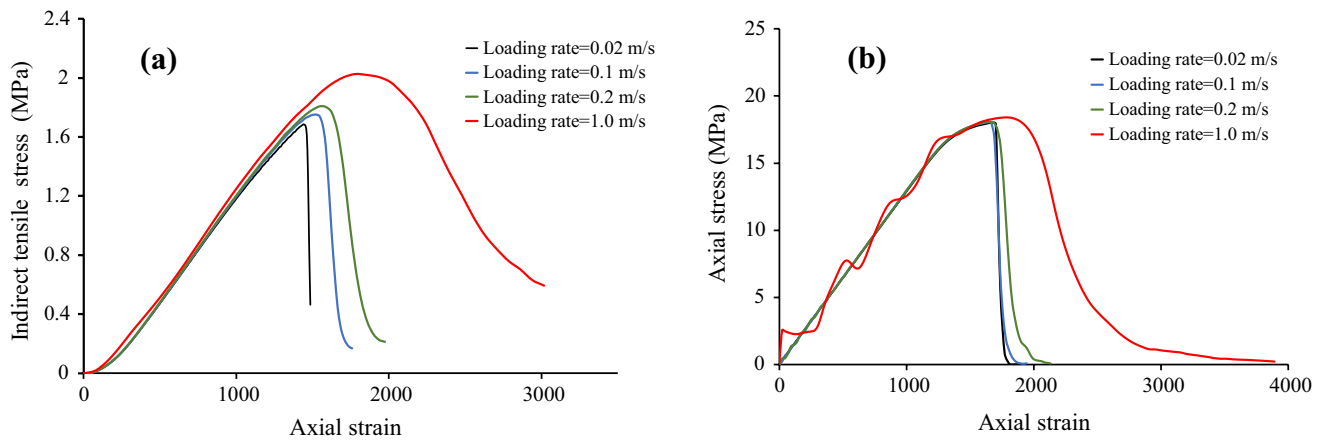


**Fig. 12** Effects of loading rates on stress–strain curves: **a** indirect tensile stress versus axial strain curves from the simulation of the BTS tests under various loading rates and **b** axial stress versus axial strain curves from the simulation of the UCS tests under various loading rates

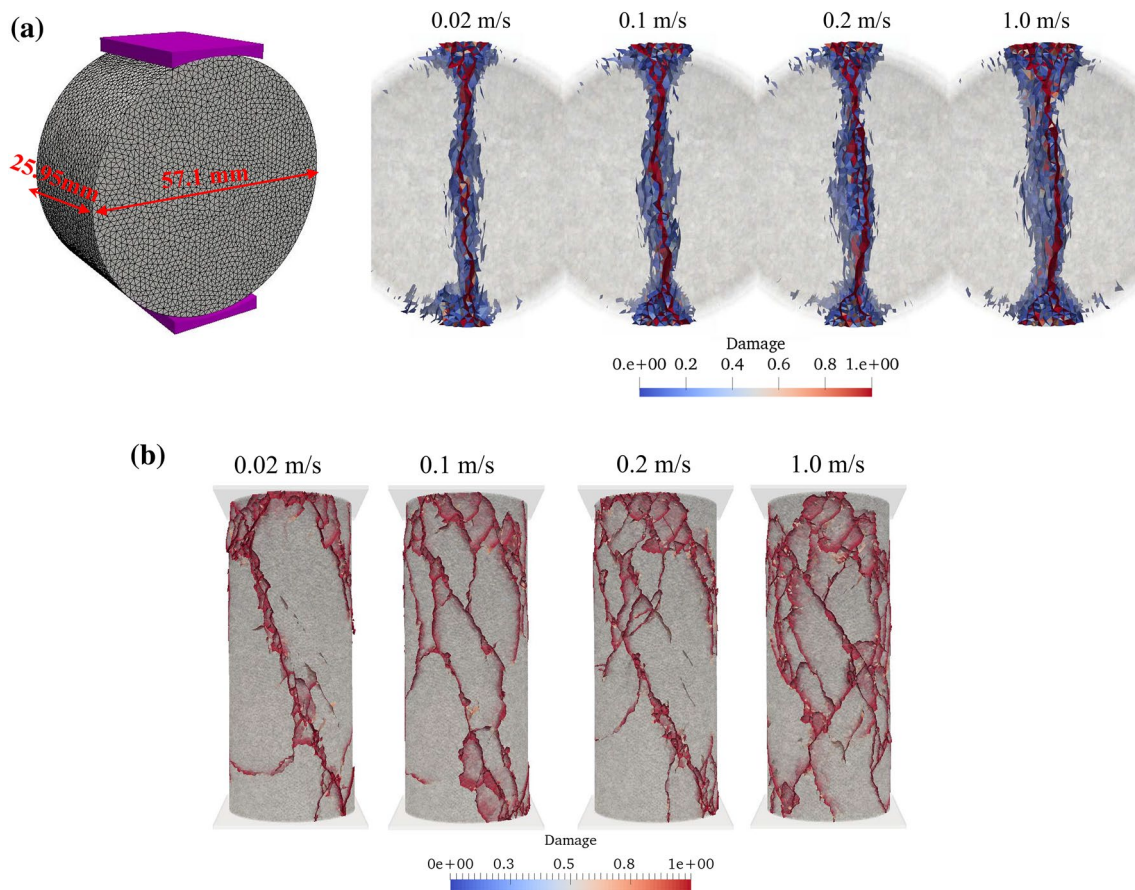


**Fig. 13** Effects of loading rates on final fracture patterns: **a**) numerical model and corresponding fracture patterns from the simulation of the BTS tests under various loading rates and **b**) fracture patterns from the simulation of the UCS tests under various loading rates

stress–strain curves (especially peak stress and post peak curve) and fracture patterns, which reveals that the application of high loading rates in some literatures may not satisfy the quasi-static loading condition. On the other hand, small

loading rate increases the simulation time significantly and the parallelization scheme such as the GPGPU parallelization together with the adaptive contact activation approach becomes necessary for the 3D FDEM simulations.



### 4.3 Effect of specimen sizes under constant loading platen velocity

As it is well-established that the application of cohesive elements intrinsically introduces the characteristic length scale and characteristic time [40], results of the 3D FDEM are also sensitive to the element size and loading rate since the 3D FDEM is based on the CZM for simulating rock fracture. Liu and Deng [25] investigated the effect of the model size on the 2D FDEM simulation of UCS and BTS tests using 2D Y-GEO and concluded that the strength of the specimen increases with the specimen size decreasing, which seems to be consistent with the size effect usually observed for rocks. Unfortunately, in their study, increasing element size was used to mesh the models with the specimen size increasing to reduce the computational cost. The 3D FDEM simulation is more computationally intensive than the 2D FDEM simulations. To reduce the computational time, small size samples, compared with the actual size of the sample used in experiments, are more prevalent used in 3D FDEM simulations in the literatures [22, 26]. Therefore, it is important to investigate the effect of changing the sample size without changing the element size and the loading rate using 3D FDEM models. With this motivation, the 3D FDEM simulation of the UCS test is investigated, while the element size and the loading rate are kept constant. Four rock cylinders with the diameters of 20 mm, 30 mm, 40 mm and 50 mm, and a length/diameter ratio of 2.5 were selected. They were discretized into TET4s with a nominal average size of 1.3 mm and were then loaded uniaxially with a constant loading rate of 0.1 m/s. Correspondingly, nominal strain rate is different for each sample size, i.e. smaller sample is subjected to higher strain rate. Figure 14 shows the stress–strain curve together with the final fracture patterns obtained from the 3D FDEM simulations. It can be seen that both peak strain and peak strength increase with the decrease in sample size. In addition, the fracture tends to develop more regionally in smaller specimens, while they develop diametrically along the specimen in larger specimens. Since the applied strain rate becomes higher for the smaller sample, the obtained results do show the important characteristics of the CZM in the way that the application of cohesive elements intrinsically introduces the loading rate dependency, i.e. strength increase with higher applied strain rate [40]. Therefore, it is questionable to calibrate the input parameters for the 3D FDEM simulations against small size specimen without carefully scaling the loading rate, i.e. when the sample size is changed, the speed of loading platen must be carefully calibrated. The most important indication here is that the strength increases as shown in Fig. 14 with the decrease in specimen size and is not caused by the size effect of CZM but rather caused by the loading rate effect of CZM. Thus, obtained results must not be misunderstood as the modelling of size effect usually observed in rocks.

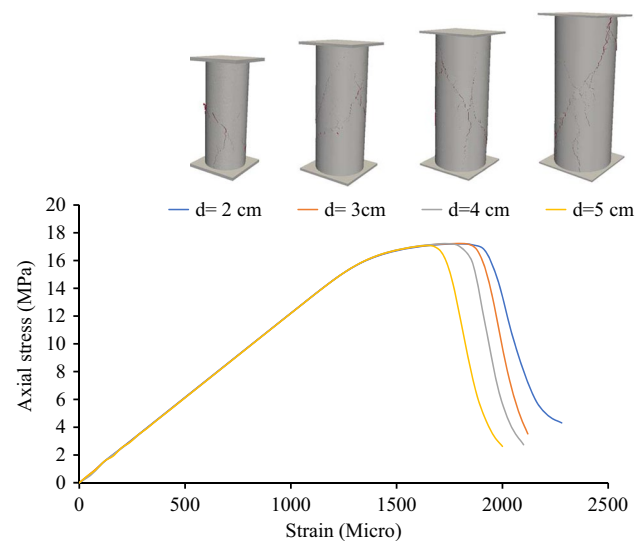


**Fig. 14** Stress–strain curve and fracture pattern from the simulation of the UCS test of rock specimens with different sizes ( $d$  is the diameter of the rock specimens)

## 5 Conclusion

FDEM has become a very useful numerical tool to simulate rock fracturing process in recent decades. Although 2D FDEM has been extensively calibrated against experimental data and used to simulate rock engineering problems by an increasing number of researchers, the study on 3D FDEM, especially the 3D FDEM simulation of the fracturing process of rocks under quasi-static loading condition, is very limited, which is, without any doubt, due to the very intensive computation of the 3D FDEM. Thanks to the parallelization, the self-developed GPGPU-parallelized Y-HFDEM 3D IDE code is able to three-dimensionally model the complex fracturing process of rocks under various loading conditions which would not be possible if a sequential FDEM code is used. However, due to the nature that FDEM is based on explicit dynamics, further speedups are needed for 3D FDEM to model the fracture of rocks involving in long time scale, such as the fracture of rock under static and quasi-static loading conditions. Correspondingly, an adaptive contact activation approach and a mass scaling technique with critical viscous damping are implemented into the GPGPU-parallelized Y-HFDEM 3D IDE to further speed up 3D FDEM simulations. A series of 3D UCS modelling is then conducted using the GPGPU-parallelized Y-HFDEM 3D IDE and the obtained results are compared to check the effects of the adaptive contact activation approach, the full contact activation approach and the mass scaling techniques with various mass scaling coefficients. It is found that the stress–strain curve and fracture pattern obtained using the adaptive and full contact activation approaches

show negligible differences but the modelling with the adaptive contact activation approach is 10.8 times faster than that with the full contact activation approach. Therefore, for static and quasi-static loading conditions, the adaptive contact activation approach can be implemented to further speed up 3D FDEM besides the parallelization. However, the occurrence of spurious/unstable modes should be carefully checked depending on the target problems, especially those under dynamic loading conditions. Moreover, it is noted that the effect of the mass scaling coefficient is not significant if it is less than 100. Thus, at least 25 times of further speedups can be achieved by the mass scaling technique although further higher times of speedups are possible with bigger mass scaling coefficients, in which the obtained results are more and less affected. After that, the selection of the contact penalty and artificial stiffness of the cohesive elements in the GPGPU-parallelized Y-HFDEM 3D IDE is analysed. It is found that in order to reasonably capture the intact behaviour of rocks using 3D FDEM, the opening, tangential and overlapping artificial stiffnesses of cohesive elements must be chosen high enough, i.e. about 100–1000 times of the elastic modulus of the modelled rocks, while the contact penalty can be chosen much lower, i.e. about 1–10 times of the elastic modulus of the modelled rocks. Moreover, taking the advantage of the drastic speedups of the adaptive contact activation approach and the mass scaling approach with critical viscous damping, the GPGPU-parallelized Y-HFDEM 3D IDE is applied to model the fracture process of rocks in triaxial compression tests under various confining pressures. The obtained axial stress–axial strain curves, axial stress–radial strain curves, volumetric strain–axial strain curve and rock fracture processes are compared with those from laboratory observations in the literatures and good agreements are found between them. The obtained peak strengths under various confining pressures are also quantitatively analysed against the Mohr–Coulomb theoretical model. It is concluded that the 3D FDEM has simulated all important characteristics of rocks in triaxial compression tests under various confining pressures such as the increase in rock compressive strength and strain at peak stress, softening behaviour for relatively lower confining pressure, transition from brittle to ductile behaviours and resulted failure patterns with the increase in confining pressure. Finally, the effects of meshes, loading rates and specimen sizes are discussed. It is found that the mixed-mode I–II fractures are highly possible, i.e. very reasonable, failure mechanisms when unstructured meshes are used in the 3D FDEM simulation. For modelling quasi-static loading conditions using the 3D FDEM, the loading rate should be smaller than 0.2 m/s to avoid significant effects of the loading rate. Therefore, it can be concluded that the adaptive contact activation approach and the mass scaling technique can further significantly speed up the 3D FDEM

modelling besides the GPGPU parallelization and the further speeding-up Y-HFDEM 3D IDE is able to simulate the complicated fracturing process of rocks under quasi-static loading conditions.

**Acknowledgements** The corresponding author would like to acknowledge the support of the Australia-Japan Foundation (Grant No. 17/20470). The second author of this work is supported by Japan Society for the Promotion of Science KAKENHI (Grant No. JP18K14165) for Grant-in-Aid for Young Scientists, which is greatly appreciated. Moreover, all authors would like to thank the guest editor, i.e. Dr Esteban Rougier, the editor in chief and the anonymous reviewers for their constructive comments and encouragements.

## Compliance with ethical standards

**Conflict of interest** On behalf of all authors, the corresponding author states that there is no conflict of interest.

## References

1. Akram MS, Sharrock G, Mitra R (2010) Physical and numerical investigation of conglomeratic rocks. Ph. D. Thesis, University of New South Wales, Sydney, Australia
2. An HM, Liu HY, Han H, Zheng X, Wang XG (2017) Hybrid finite-discrete element modelling of dynamic fracture and resultant fragment casting and muck-piling by rock blast. *Comput Geotech* 81:322–345
3. Baumgarten L, Konietzky H (2013) Investigations on the fracture behaviour of rocks in a triaxial compression test. In: ISRM international symposium-EUROCK 2013. International Society for Rock Mechanics and Rock Engineering
4. Bažant ZP, Shang-Ping B, Ravindra G (1993) Fracture of rock: effect of loading rate. *Eng Fract Mech* 45:393–398
5. Camacho GT, Ortiz M (1996) Computational modelling of impact damage in brittle materials. *Int J Solids Struct* 33:2899–2938
6. Chen S, Wei C, Yang T, Zhu W, Liu H, Ranjith PG (2018) Three-dimensional numerical investigation of coupled flow-stress-damage failure process in heterogeneous poroelastic rocks. *Energies* 11:1923
7. Egert R, Seithel R, Kohl T, Stober I (2018) Triaxial testing and hydraulic-mechanical modeling of sandstone reservoir rock in the Upper Rhine Graben. *Geotherm Energy* 6:23
8. Euser B, Lei Z, Rougier E, Knight EE, Frash L, Carey JW, Viswanathan H, Munjiza A (2018) 3-D finite-discrete element simulation of a triaxial direct-shear experiment. In: 52nd U.S. rock mechanics/geomechanics symposium. American Rock Mechanics Association, Seattle, Washington, p 6
9. Fukuda D, Mohammadnejad M, Liu H, Cho S, Oh S, Min, G, Chan A, Kodama J, Fujii F (2018) GPGPU-based 3-D hybrid FEM/DEM for numerical modelling of various rock testing methods. In: 12th Australia and New Zealand Young geotechnical professionals conference, pp 1–10
10. Fukuda D, Mohammadnejad M, Liu H, Dehkoda S, Chan A, Cho S-H, Min G-J, Han H, Kodama J-I, Fujii Y (2019) Development of a GPGPU-parallelized hybrid finite-discrete element method for modeling rock fracture. *Int J Numer Anal Methods Geomech* 43:1797–1824
11. Fukuda D, Mohammadnejad M, Liu H, Zhang Q, Zhao J, Dehkoda S, Chan A, Kodama J, Fujii Y (2019) Development of a 3D hybrid finite-discrete element simulator based on GPGPU-parallelized computation for modelling rock fracturing under

- quasi-static and dynamic loading conditions. *Rock Mech Rock Eng.* <https://doi.org/10.1007/s00603-019-01960-z>
12. Gao FQ, Stead D (2014) The application of a modified Voronoi logic to brittle fracture modelling at the laboratory and field scale. *Int J Rock Mech Min Sci* 68:1–14
  13. Goodman RE (1989) *Introduction to rock mechanics*. Wiley, New York
  14. Guo L, Xiang J, Latham JP, Izzuddin B (2016) A Numerical investigation of mesh sensitivity for a new three-dimensional fracture model within the combined finite-discrete element method. *Eng Fract Mech* 151:70–91
  15. Guo L (2014) *Development of a three-dimensional fracture model for the combined finite-discrete element method*. Imperial College London, London
  16. Ha J, Grasselli G (2018) Three-dimensional FDEM modelling of laboratory tests and tunnels. In: 52nd U.S. rock mechanics/geomechanics symposium. American Rock Mechanics Association, Seattle, Washington, p 8
  17. Hamdi P (2015) *Characterization of brittle damage in rock from the micro to macro scale*. Science: Department of Earth Sciences
  18. Heinze T, Jansen G, Galvan B, Miller SA (2016) Systematic study of the effects of mass and time scaling techniques applied in numerical rock mechanics simulations. *Tectonophysics* 684:4–11
  19. Horii H, Nemat-Nasser S (1986) Brittle failure in compression: splitting faulting and brittle-ductile transition. *Philos Trans R Soc Lond Ser A Math Phys Sci* 319:337–374
  20. ISRM (1978) Suggested methods for determining the uniaxial compressive strength and deformability of rock materials. *Int J Rock Mech Min Sci* 16:137–140
  21. Jaime MC (2011) *Numerical modeling of rock cutting and its associated fragmentation process using the finite element method*. University of Pittsburgh, Pittsburgh
  22. Lisjak A, Mahabadi OK, He L, Tatone BSA, Kaifosh P, Haque SA, Grasselli G (2018) Acceleration of a 2D/3D finite-discrete element code for geomechanical simulations using general purpose GPU computing. *Comput Geotech* 100:84–96
  23. Liu HY, Kang YM, Lin P (2015) Hybrid finite-discrete element modeling of geomaterials fracture and fragment muck-piling. *Int J Geotech Eng* 9:115–131
  24. Liu HY, Han H, An HM, Shi JJ (2016) Hybrid finite-discrete element modelling of asperity degradation and gouge grinding during direct shearing of rough rock joints. *Int J Coal Sci Technol* 3(3):295–310
  25. Liu Q, Deng P (2019) A numerical investigation of element size and loading/unloading rate for intact rock in laboratory-scale and field-scale based on the combined finite-discrete element method. *Eng Fract Mech* 211:442–462
  26. Mahabadi O, Kaifosh P, Marschall P, Vietor T (2014) Three-dimensional FDEM numerical simulation of failure processes observed in Opalinus Clay laboratory samples. *J Rock Mech Geotech Eng* 6:591–606
  27. Mahabadi OK, Lisjak A, Munjiza A, Grasselli G (2012) Y-Geo: new Combined finite-discrete element numerical code for geomechanical applications. *Int J Geomech* 12:676–688
  28. Mardalizad A, Scazzosi R, Manes A, Giglio M (2018) Testing and numerical simulation of a medium strength rock material under unconfined compression loading. *J Rock Mech Geotech Eng* 10:197–211
  29. Mohammadnejad M, Liu H, Chan A, Dehkhoda S, Fukuda D (2018) An overview on advances in computational fracture mechanics of rock. *Geosyst Eng* 7:1–24
  30. Mohammadnejad M, Liu H, Dehkhoda S, Chan A (2017) Numerical investigation of dynamic rock fragmentation in mechanical cutting using combined FEM/DEM. In: 3rd nordic rock mechanics symposium—NRMS 2017. International Society for Rock Mechanics and Rock Engineering, Helsinki, Finland
  31. Munjiza A (1992) *Discrete elements in transient dynamics of fractured media*. Ph.D. thesis, Swansea University, UK
  32. Munjiza A (2004) *The combined finite-discrete element method*. Wiley, Chichester
  33. Munjiza A, John NWM (2002) Mesh size sensitivity of the combined FEM/DEM fracture and fragmentation algorithms. *Eng Fract Mech* 69:281–295
  34. Munjiza A, Knight EE, Rougier E (2011) *Computational mechanics of discontinua*, 1st edn. Wiley, London
  35. Munjiza A, Owen DRJ, Bicanic N (1995) A combined finite-discrete element method in transient dynamics of fracturing solids. *Eng Comput* 12:145–174
  36. Munjiza A, Rougier E, Knight EE (2015) *Large strain finite element method: a practical course*, 1st edn. Wiley, London
  37. Paterson MS, Wong T-F (2005) *Experimental rock deformation—the brittle field*. Springer, Berlin
  38. Rougier E, Knight EE, Broome ST, Sussman AJ, Munjiza A (2014) Validation of a three-dimensional Finite-Discrete Element Method using experimental results of the Split Hopkinson Pressure Bar test. *Int J Rock Mech Min Sci* 70:101–108
  39. Rougier E, Knight EE, Sussman AJ, Swift RP, Bradley CR, Munjiza A, Broome ST (2011) *The combined finite-discrete element method applied to the study of rock fracturing behavior in 3D*. American Rock Mechanics Association, New York
  40. Ruiz G, Ortiz M, Pandolfi A (2000) Three-dimensional finite-element simulation of the dynamic Brazilian tests on concrete cylinders. *Int J Numer Methods Eng* 48:963–994
  41. Santarelli FJ, Brown ET (1989) Failure of three sedimentary rocks in triaxial and hollow cylinder compression tests. *Int J Rock Mech Min Sci Geomech Abstr* 26:401–413
  42. Solidity (2017) Solidity Project. <http://solidityproject.com/>. Accessed 14 Nov 2018
  43. Tan X, Konietzky H, Frühwirt T (2015) Numerical simulation of triaxial compression test for brittle rock sample using a modified constitutive law considering degradation and dilation behavior. *J Central South Univ* 22:3097–3107
  44. Tatone BSA (2014) *Investigating the evolution of rock discontinuity asperity degradation and void space morphology under direct shear*. University of Toronto (Canada)
  45. Tatone BSA, Grasselli G (2015) A calibration procedure for two-dimensional laboratory-scale hybrid finite-discrete element simulations. *Int J Rock Mech Min Sci* 75:56–72
  46. Turichshev A, Hadjigeorgiou J (2016) Triaxial compression experiments on intact veined andesite. *Int J Rock Mech Min Sci* 86:179–193
  47. Turon A, Dávila CG, Camanho PP, Costa J (2007) An engineering solution for mesh size effects in the simulation of delamination using cohesive zone models. *Eng Fract Mech* 74:1665–1682
  48. Xie J, Waas AM, Rassaian M (2016) Estimating the process zone length of fracture tests used in characterizing composites. *Int J Solids Struct* 100–101:111–126
  49. Yan C, Jiao Y-Y (2018) A 2D fully coupled hydro-mechanical finite-discrete element model with real pore seepage for simulating the deformation and fracture of porous medium driven by fluid. *Comput Struct* 196:311–326
  50. Yan C, Jiao Y-Y, Zheng H (2018) A fully coupled three-dimensional hydro-mechanical finite discrete element approach with real porous seepage for simulating 3D hydraulic fracturing. *Comput Geotech* 96:73–89
  51. Zhang Z, Paulino GH, Celes W (2007) Extrinsic cohesive modeling of dynamic fracture and microbranching instability in brittle materials. *Int J Numer Methods Eng* 72:893–923